

Sunlight penetration dominates the thermal regime and energetics of a shallow ice-covered lake in arid climate

Wenfeng Huang^{1,2*}, Wen Zhao¹, Cheng Zhang¹, Matti Leppäranta³, Zhijun Li^{4*}, Rui Li¹, Zhanjun Lin²

1 Key Laboratory of Subsurface Hydrology and Ecological Effects in Arid Region (the Ministry of Education), Chang'an University, Xi'an, China

2 State Key Laboratory of Frozen Soil Engineering, Northwest Institute of Eco-Environment and Resources, Chinese Academy of Science, Lanzhou, China

3 Institute of Atmospheric and Earth Sciences, University of Helsinki, Helsinki, Finland.

4 State Key Laboratory of Coastal and Offshore Engineering, Dalian University of Technology, Dalian, China

*Correspondence to: Wenfeng Huang (huangwenfeng@chd.edu.cn) and Zhijun Li (lizhijun@dlut.edu.cn)

Abstract. The Mongolian Plateau is characterized by cold and arid winter with very little precipitation (snowfall), strong solar insolation, and dry air. But little is known about the thermal regimes of ice and ice-covered lakes and their response to the distinct weather and climate in this region. In a typical large, shallow lake, ice/snow processes(cover) and under-ice thermodynamics were monitored for four winters in 2015–2019. Heat transfer at the ice-water interface and lake heat budget were investigated. The results revealed that persistent bare ice of 35–50 cm permits 20–35% of incident solar radiation to get transmitted into the under-ice water, providing the source for under-ice energy flows and causing/maintaining high water temperature (up to 6–8°C) and high heat flux from water to ice (averages of 20–45 W m⁻²) in mid-winter along with higher heat conduction in the ice interior during freezing. The heat balance shows that the transmitted radiation and the heat flux from water to ice are the dominant and highly correlated heat flows in the lake. Both bulk water temperature and temperature structure are sensitive to solar transmittance and occasional snow events. Under-ice convective mixing does not necessarily occur because of stratification of salinity in the water body. Especially, salt exclusion in freezing changes both the bulk salinity and the salinity profile that plays a major role in the stability and mixing of the water column in this shallow lake.

1 Introduction

Lakes are important water resources and provide vital habitats for aquatic ecosystems. More than 55% of world lakes are located between 40 and 80°N in the northern hemisphere (Verpoorter et al., 2014) and have potential to freeze seasonally (Kirillin et al., 2012), especially in Arctic, boreal, and temperate climate, and high mountain regions. Due to distinct properties of ice compared to water, seasonal formation and decay of ice cover have tremendous impacts on the lake water quality (Yang et al., 2016), physical and chemical conditions (Yang et al., 2021; Cavaliere and Baulch, 2018; Huang et al., 2019a), aquatic ecosystem (Griffiths et al., 2017; Song et al., 2019), and land-atmosphere mass and heat interaction (Wang et al., 2015; Franz et al., 2018). Therefore, common concerns have been widely spread on mapping lake ice physics and its underlying physical mechanisms in the evolution of ice seasons.

39 Field and modeling investigations on lake ice processes have a long history in northern temperate and
40 boreal regions, such as Fennoscandia, central Europe, northern Canada, and the Great Lakes. Shortening
41 of ice cover period has been documented currently in lakes in these northern regions (Bernhardt et al.,
42 2012; Lei et al., 2012; Karetnikov et al., 2017; Ptak et al., 2020). However, the lake ice regime has
43 remained less studied due to lack of long-term observational records in arid climate regions, such as
44 central Asia and high mountains, which are subject to a quite different landscape, regional climate, and
45 hydrological cycles compared with the northern temperate, boreal, and Arctic environment.

46 Lake thermal stratification is of great importance to hydrodynamics and transport of nutrients, oxygen,
47 and primary production, which influence limnological habitats and ecosystems. In freezing freshwater
48 lakes, stable inverse thermal stratification usually forms and persists under the ice cover with the
49 temperature smaller than the maximum density temperature (3.98°C). After the onset of melting, strong
50 solar irradiance can penetrate the ice cover into the water and drive turbulent convection (Bouffard et al.,
51 2019; Volkov et al., 2019) until the bulk temperature reaches or surpasses the maximum density
52 temperature or until breakup (Yang et al., 2020). However, in some shallow mid-latitude brackish lakes,
53 this is not the story. During melting period, a warm middle layer may form due to salinity stratification
54 and separate the overlying inverse thermal stratification and the underlying positive thermal stratification.
55 The temperature of this warm layer can go up to around 10°C before the breakup (e.g. Huang et al.,
56 2019b; Kirillin et al., 2021). This underlines the uniqueness of seasonally ice-covered lakes in mid-
57 latitude arid regions and the importance of their different climate. It still remains unclear how this
58 stratification forms and evolves and how it interacts with the snow/ice cover.

59 After freeze-up, the ice cover shelters the lake from atmospheric forcing and deposits. The lake boundary
60 constitutes of only the ice cover on the top and sediment at the bottom. The heat budget is governed by
61 radiative and sensible fluxes across the ice-water-sediment interfaces (Leppäranta, et al., 2019). But these
62 fluxes, including solar radiation transfer, ice-water heat exchange, and sediment heat release, have not
63 been well quantified in mid-latitude arid region lakes. Especially, the ice-water heat flux, a key factor
64 affecting the mass and energy balance of both ice and water, has been demonstrated to be remarkably
65 higher in Central Asia than in Arctic and boreal zones (Malm et al., 1997; Jakkila et al., 2009; Huang et
66 al., 2019a,b; Lu et al., 2020). But the regime underpinning its high values is still unknown.

67 To fill the knowledge gaps in winter thermodynamics of lakes in cold and arid Asia and their background
68 energy flows, we performed a four-winter observation program of snow/ice processes, solar radiation
69 transfer, and temperature profiles of air-ice-water-sediment column in a typical large shallow lake that is
70 seasonally ice-covered for 4–5 months, located in the southern border of the Mongolia Plateau. Below,
71 observations and models are combined 1) to reveal the seasonal and diurnal dynamics of the temperature
72 stratification under ice in the mid-latitude arid climate, and 2) to quantify and balance the involved heat
73 fluxes that determine the thermal state of the lake.

74 **2 Data and methods**

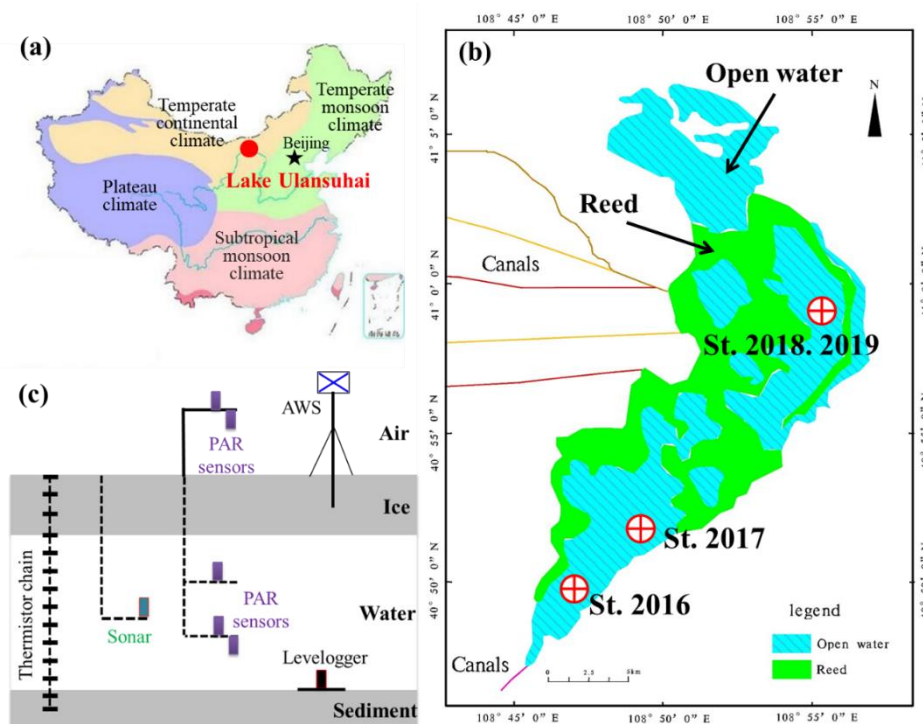
75 **2.1 Study site**

76 The Hetao Basin (ca. 6,000 km², mean altitude > 1,000 m), one of the oldest and largest irrigation areas
77 in China, is located in the central southern Mongolian Plateau controlled by temperate continental climate.
78 In the Hetao Basin, the annual sunshine duration is 3,000–3,200 h, the annual air temperature is 5.6–
79 7.4°C with the lowest and highest monthly temperature of –14– –11°C (Jan) and 22–24°C (Jul), the frost-
80 free period is 130–150 d, and the annual precipitation is 150–400 mm concentrated in the warm season.
81 Most parts of the basin have been desertified or semi-desertified in recent decades.

82 Lake Ulansuhai (40°36′–41°03′N, 108°41′–108°57′E, altitude 1,019 m) is a typical large, shallow lake
 83 in desert/semi-desert region with a total area of about 306 km² (Fig. 1). It is a very important part of the
 84 irrigation and drainage system of the Hetao Basin, and its major water source comes from the farmland
 85 irrigation drainage and domestic sewage. The maximum and mean depths are 2.5–3.0 m and 1.0–1.5 m,
 86 respectively. The annual air temperature, hours of sunshine, precipitation, evaporation, wind speed,
 87 frost-free period are 7.3°C, 3,185 h, 224 mm, 1,502 mm, 3.5 m s⁻¹, and 152 d, respectively (Sun et al.,
 88 2011). The solar noon-time and altitude in winter are 12:45±15 min and 41±10°, respectively. The ice
 89 cover is usually free of snow or only sparsely snow-covered due to occasional snowfall events and
 90 strong winds.

91 The lake surface elevation is regulated through pumping water from the Yellow River via the main
 92 inflow canal at the western shore. The total annual water supply is approximately 4×10^8 m³,
 93 equivalent to the lake volume. But in winter (Nov–Mar), very little surface inflow/outflow exists
 94 except possible minor wastewater inflow (Sun et al., 2013), and the subsurface inflow is also negligible
 95 (Zhu et al., 2014). For more detailed information, please consult Lu et al. (2020) and references therein.
 96 According to our sampling tests in winter 2017, the lake water is brackish or weakly saline with
 97 salinity of 1.0–1.5‰ before the ice-on and gradually increasing to 2.5–3.0‰ due to exclusion of salts
 98 when the ice grows to its annual maximum.

99 Due to its unique climate and eutrophication, the lake ecology under the ice cover is very active with
 100 high rates of primary production and respiration. This is believed to be highly related to the under-ice
 101 solar irradiance and temperature and the key role of ice and snow processes (Song et al., 2019; Huang
 102 et al., 2021). Our previous observations revealed the mass and heat balance of the lake ice cover and
 103 the impacts of warm water under the ice cover (Lu et al., 2020), but further investigations were
 104 performed and combined here to look into the thermal stratification regimes.



105
 106 **Figure 1. Locations of Lake Ulansuhai (a) and study sites (b) and the field instrumentation (c). In**
 107 **each winter, a thermistor chain was refrozen into ice cover to measure temperature profile of the**
 108 **air-ice-water-sediment column with an established automatic weather station (AWS); more than 3**

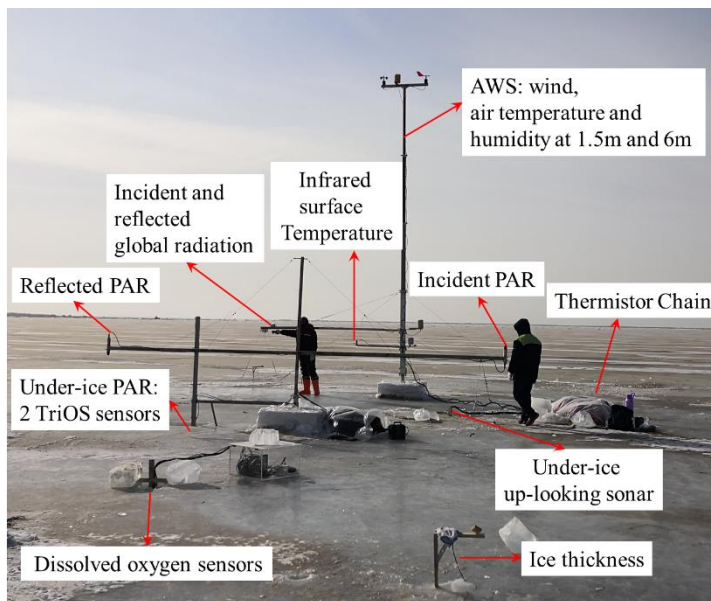
109 radiation sensors over photosynthesis active radiation (PAR) band were deployed to observe the
 110 incident, reflected and transmitted solar radiation.

111

112 2.2 Data acquisition

113 During winters of 2015-2019, field campaigns were conducted in open, reed-free areas of Lake Ulansuhai
 114 (Figs. 1c and 2). In each winter, an automatic weather station (AWS) was established on the ice cover, to
 115 record wind speed and direction, air temperature and humidity, incident and reflected global radiation
 116 (300–3000 nm), and the skin temperature of the ice/snow surface. An under-ice uplooking sonar (WUUL-
 117 1/2, Wuhan University, China) was used to measure the ice thickness evolution with the accuracy of 2
 118 mm. Snow thickness was measured manually using a snow stake every 1–2 days. The temperature profile
 119 of the air-ice-water-sediment column was observed using a thermistor chain (PTWD, Jinzhou Sunshine
 120 Technology Co. Ltd, China) at 5–10 cm spacing with the accuracy of 0.05°C. TriOS spectral radiometers
 121 with the accuracy of 0.04–0.06 mW m⁻² nm⁻¹ (RAMSES-ACC-VIS, TriOS, German) were used to
 122 measure the incident and reflected photosynthetically active radiation (PAR) over the ice/snow surface
 123 and under the ice cover. The water level was monitored using a temperature-pressure logger with an
 124 accuracy of 0.05% (LTC Levellogger, Solinst, Canada) placed 20 cm above the sediment surface. All the
 125 above variables were recorded every 10 min. Information of the acquired datasets is summarized in Table
 126 1 (see also Huang et al. 2021).

127 In the winter of 2017, the under-ice water electric conductivity (EC) was measured using 3 online
 128 conductivity loggers (HOBO U24, Onset, USA, accuracy of 3%) at depths of 60 cm, 100 cm, and 150
 129 cm from Jan 21 to Mar 11 (Table 1). Concurrently, ice and water samples with 5 cm spacing were
 130 collected 8 times this winter to measure their EC and salinity using a portable YSI salinometer with
 131 accuracy of 1%.



132

133 **Figure 2. Field setup of apparatus deployed and corresponding monitored variables in winter of**
 134 **2019**

135 **Table 1. Data series acquired during the four-winter observation program**

Winter	2016	2017	2018	2019
Available	Jan 11–Mar 9	Jan 21–Mar 11	Jan 9–Feb 25	Jan 20–Feb 27

duration				
Water depth	220 cm	170 cm	143 cm	140 cm
Ice/snow thickness	√	√	√	√
Air-ice-water-sediment temperature	5 cm spacing in ice, 10–15 cm spacing in water and sediment	5 cm spacing in ice, 5–10 cm spacing in water and sediment	5 cm spacing in ice, 5–10 cm spacing in water and sediment	5 cm spacing in ice, 10 cm spacing in water and sediment
Under-ice irradiation	175 cm	80 cm, 130 cm	65 cm, 90 cm, 120 cm	80 cm, 120 cm
Under-ice upwelling radiation		105 cm	100 cm	
Water level		√		
Electric Conductivity		60 cm, 100 cm, 150 cm		

136 Note: the observed depths for under-ice irradiation and upwelling radiation and electric conductivity
 137 denote the distances below the ice surface.

138 2.3 Heat flux calculation and balance

139 In freshwater lakes, the water temperature is colder than 3.98°C with a weak inverse thermal stratification
 140 during freezing (Winter I stage), and typically a convective mixing layer forms between the top cold
 141 interfacial layer and the warm quiescent layer during melting (Winter II stage) (Kirillin et al., 2012). The
 142 stratification structure in Lake Ulansuhai was checked using temperature gradient following Kirillin et
 143 al. (2018).

144 After freeze-up, as illustrated in Fig. 3, the thermal regime of the water column is governed by the solar
 145 irradiance penetrating through the ice cover (R_w), solar radiation absorbed by the lake sediment (if any)
 146 (R_{sed}), heat fluxes through ice-water (F_w) and water-sediment (F_{sed}) interfaces, and horizontal heat gain
 147 by advection and diffusion (F_h) from the neighboring water body. If the zero-reference level for heat is
 148 defined as the heat content of liquid fresh water at its freezing point temperature, the heat content of
 149 water is $\rho_w c_w T_w h_w$, and the heat budget of a water column is

$$150 R_w - R_{sed} + F_{sed} + F_h - F_w = \rho_w c_w h_w \frac{dT_w}{dt} + \rho_w c_w T_w \frac{dh_w}{dt}, \quad (1)$$

151 where ρ_w , c_w , and T_w are the density, specific heat, and bulk temperature of water, respectively. Other
 152 variables are defined in Fig. 3. The lateral heat transport F_h is negligible in this shallow lake with a flat
 153 bottom (Rizk et al., 2014; Kirillin et al., 2015). The two terms on the right-hand side are the heat content
 154 changes induced by changes in the water temperature and depth, respectively. The water level logger
 155 indicated that the lake lost water through seepage to soil quite slowly (about 0.6 mm/d) during ice seasons,
 156 and the heat loss due to the bottom water seepage was estimated to be smaller than 0.8 W m⁻² and thus
 157 was ignored as a minor term compared to the other heat fluxes.

158 *Under-ice solar irradiance.* The light extinction coefficient of the under-ice water was measured as 2.1
 159 m⁻¹ under a clear sky on Jan 7, 2018. Using the observed irradiance by under-ice spectral sensors, the
 160 solar irradiance at the ice-water interface (R_w) was derived from a one-band exponential decay law of
 161 light transfer in water column, following

162 $R_w = R_d \exp(\kappa_w(z_d - h_i)), \quad (2)$

163 where R_d is the observed downward irradiance at depth z_d , h_i is the ice thickness, and κ_w is the light
164 extinction coefficient of water.

165 *Sediment heat flux.* The heat exchange flux through the water-sediment interface (F_{sed}) was calculated
166 with the gradient method,

167
$$F_{sed} = -\kappa_{sed} \left. \frac{\partial T_{sed}}{\partial z} \right|_{bottom} \approx -\kappa_{sed} \frac{\Delta T_{sed}}{\Delta z}, \quad (3)$$

168 where κ_{sed} is the thermal conductivity of sediment and T_{sed} is the observed sediment temperature. In the
169 winter of 2018, four thermistors were buried in the sediment (1 cm, 9cm, 17 cm, and 30 cm below the
170 sediment surface) to measure the sediment temperature profiles. Assuming the heat transfer in the top
171 sediment is governed by the typical one-dimensional vertical heat conduction equation, an optimal
172 control model was deployed to retrieve the effective thermal diffusivity of the sediment was estimated
173 based on the observed sediment temperature profiles. For details on the optimal control model, please
174 refer to Shi et al. (2014). The thermal conductivity can be determined ($0.2\text{--}0.7 \text{ W m}^{-1}\text{C}^{-1}$) with measured
175 density and specific heat capacity of sediment. $\kappa_{sed} = 0.5 \text{ W m}^{-1}\text{C}^{-1}$ was used in Eq. 3.

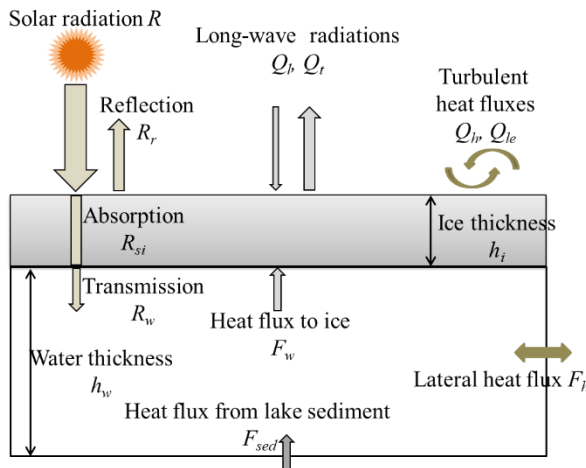
176 *Water-to-ice heat flux.* The water-to-ice heat flux can be derived from the heat balance at the ice-water
177 interface,

178
$$F_w = Q_c - Q_l = -\kappa_i \left. \frac{\partial T_i}{\partial z} \right|_{z=h_i} - \rho_i L_f \frac{\partial h_i}{\partial t}, \quad (4)$$

179 where Q_c and Q_l are the conductive heat flux to ice and the latent heat due to freezing/melting,
180 respectively, and ρ_i and L_f are the density and latent heat of fusion of ice, respectively. The first term
181 denotes the heat conduction into the ice interior, which can be derived using the temperature gradient in
182 the bottom ice layer. The second term on the right-hand side denotes the heat release/absorption due to
183 freezing/melting, which can be derived from ice thickness observations.

184 The heat content due to temperature change (i.e., the first term on the right-hand side of Eq. 1) was
185 calculated using the observed water temperature profiles.

186 Direct use of semi-hourly observed datasets brought high-frequency fluctuations in estimated heat flux,
187 and then daily means were used for further analysis of seasonal dynamics.



188
189 **Figure 3. Heat budget components of the water column under the ice (modified from Huang et al,**

190 2019b).

191

192 2.4 Potential errors in heat flux estimation

193 Potential errors in the above heat flux estimation usually come from the measurement accuracy of the
194 deployed apparatuses. The maximum error for each flux was determined based on the related apparatus
195 accuracy (Table 2). The thermistor accuracy is expected to lead to errors less than 1.7 W m^{-2} on F_s and
196 F_{T_w} , and the ice density caused errors less than 1.3 W m^{-2} on F_w . Other heat fluxes suffer to only negligible
197 uncertainties ($< 0.3 \text{ W m}^{-2}$) induced by individual sources. Errors from several sources may accumulate
198 especially in F_w , but the accumulated errors in F_w should be less than 8%.

199

200 **Table 2.** Uncertainties in calculation of heat fluxes

Error source	Errors in heat flux (W m^{-2})*			
	R_w	F_{sed}	F_w	$F_{T_w} = \rho_w c_w h_w \frac{dT_w}{dt}$
Radiation precision	0.08	–	–	–
Thermistor precision	–	0.25	1.1	1.7
Ice thickness	0.1	–	–	0.01
Ice growth rate	–	–	0.3	–
Ice density	–	–	1.25	–
Water density	–	–	–	0.2

201 * Dashes (–) indicate inapplicable.

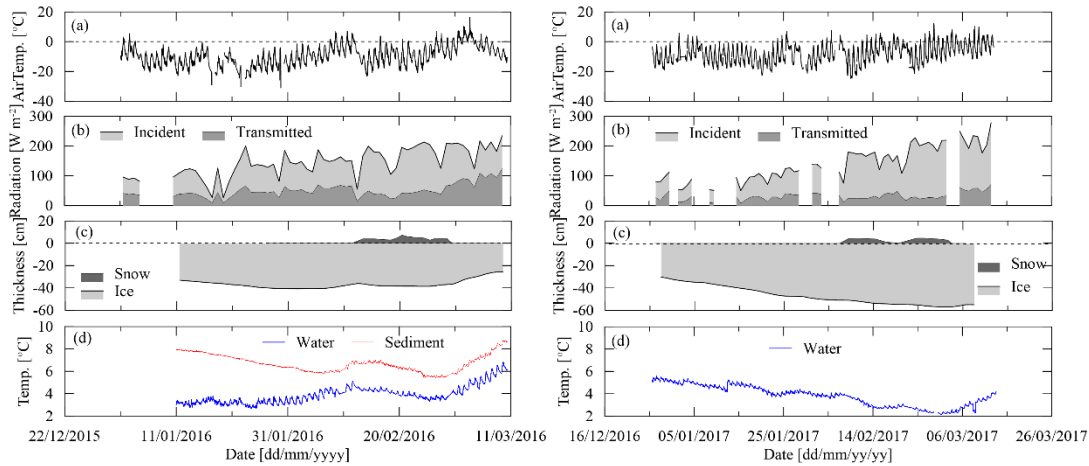
202 3 Results

203 3.1 Lake ice and temperature

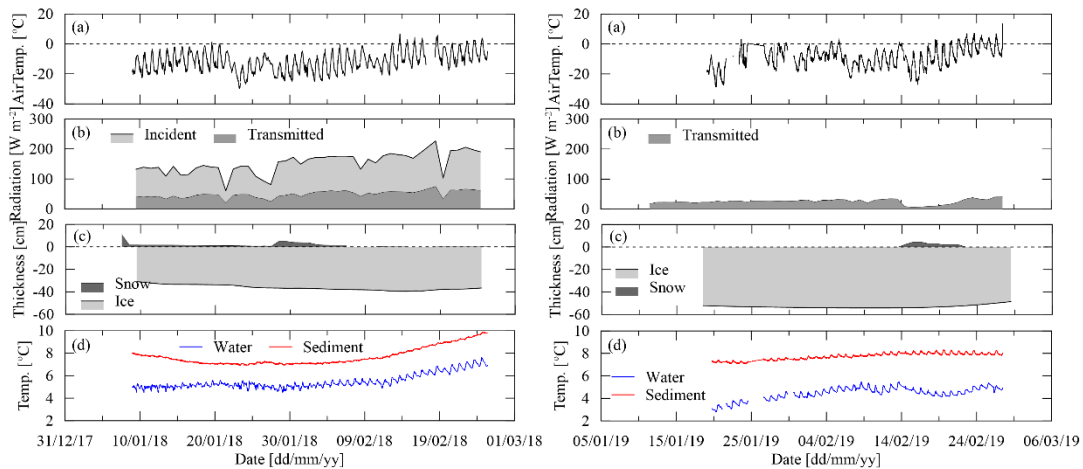
204 Our observations were conducted during mid-winter covering the turning point from ice growth to
205 melting. The air temperature was consistently lower than 0°C , but its daily amplitude was very high (10–
206 16°C) and the peak at noon/afternoon could be close to 0°C (Fig. 4). Wind speed was generally lower
207 than 4 m s^{-1} except occasional gusts that led to snow or dust drifting. The relative humidity of air 2-m
208 above the ice surface also showed an evident diurnal cycle between 40% and 80%.

209 The peak incident solar radiation was each day roughly $500\text{--}800 \text{ W m}^{-2}$, and its daily average was 80--
210 200 W m^{-2} showing an increasing trend from the beginning to the end of our observation period. But the
211 daily average was always smaller than 100 W m^{-2} due to prevailing cloudy or overcast skies in winter
212 2019. Occasional snowfalls usually brought thin snow layers ($< 6 \text{ cm}$) that continuously ablated due to
213 wind blowing and melting and sublimation. A new snow cover could increase the surface albedo up to
214 over 0.80 but this increment gradually disappeared within one week following the snowfall.

215 The maximum annual ice thickness varied between 35 cm and 60 cm, accounting for 30%–60% of the
216 mean lake depth. The bulk water temperature under ice cover was $3\text{--}7^\circ\text{C}$ and showed diurnal cycles and
217 synoptic decreases following snowfall events, evidencing the decrease of transmitted solar radiation. The
218 sediment surface layer was always warmer than the water column during the observation period, showing
219 that the sediment works as a heat source to the overlying water.



220



221

222 **Figure 4. Observational air temperature T_a (a), daily means of incident and transmitted solar**
 223 **radiation (b), snow and ice thickness (c), temperature of water column and surface sediment. (top**
 224 **left: winter 2016; top right: winter 2017; bottom left: winter 2018; bottom right: winter 2019)**

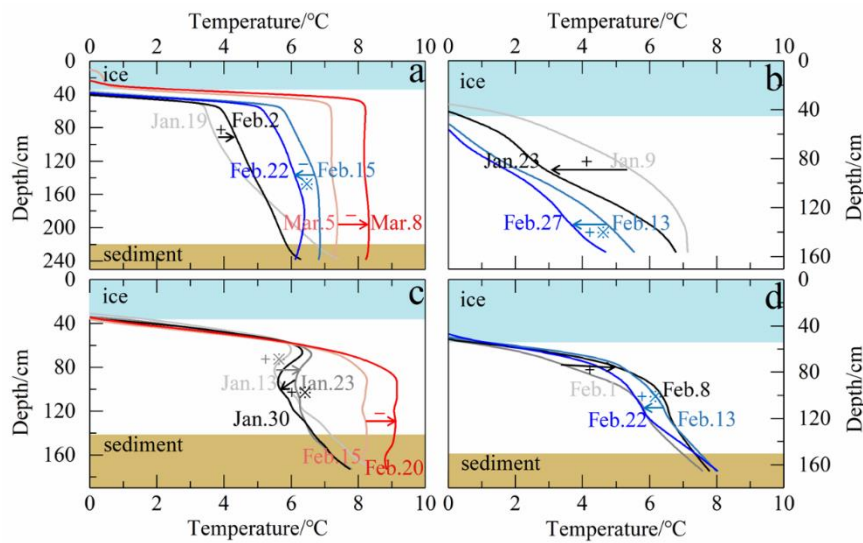
225

226 **3.2 Thermal stratification and mixing in midwinter**

227 In mid-winter, the lake sediment was still very warm with surface temperature $> 6^\circ\text{C}$, usually causing
 228 temperatures higher than 4°C in the lower part of water column (Fig. 5). It is hypothesized that this
 229 stratification was supported by salinity stratification. There is no detailed concurrent salinity profile data
 230 available, but the bulk salinity is of the order of 1‰, enriched in ice season. As was observed in the
 231 winter of 2017 (Fig. 6), stable salinity stratification existed during the freezing period, and as salt was
 232 continuously excluded to water through the ice-water interface during water freezing, the bulk salinity
 233 increased and the salinity structure approached gradually to neutral stratification. But when the ice
 234 melting began on Mar 7, the bulk salinity decreased and stable salinity stratification formed again due to
 235 fresher meltwater intrusion. The sensitivity of density to temperature is very low in the neighborhood of
 236 4°C so quite small salinity changes can compensate for the observed temperature structure for neutral
 237 density stratification. Although our observations didn't cover the whole ice season, evident seasonal and
 238 annual variations were observed.

239 A common thin layer (10–30 cm) of strong inverse stratification (i.e., interface layer) prevailed just
 240 beneath the ice due to the large difference in temperature of the ice base at the freezing point and the

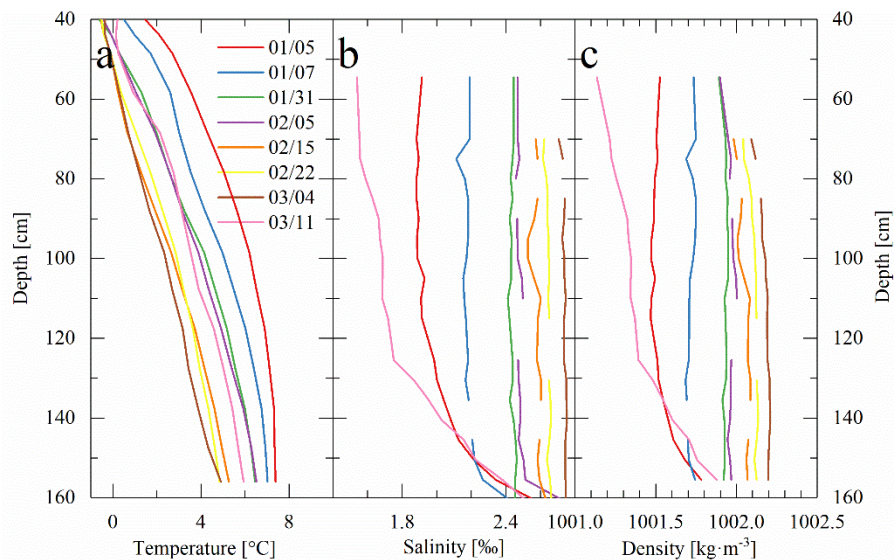
241 bulk water column, e.g. in winters 2016, 2018 and 2019. But in winter 2017, this thin top layer did not
 242 show up and a persistent thick inverse structure developed through the water column (Fig. 5b).
 243 Underneath the top cold interface layer, the temperature increased slowly downward to the warm
 244 sediment (weak inverse structure) in winter 2019 and prior to 3 Mar in winter 2016 (Fig. 5a and 5d).
 245 After 3 Mar in winter 2016 and 10 Feb in winter 2018, a thermally homogeneous convective layer
 246 developed after the bulk water temperature rose above approximately 7°C (Fig. 5a and 5c). Strikingly,
 247 before the formation of convective mixing in winter 2018, a “warm” zone of 30 cm (local maximum
 248 temperature) with temperature decreasing both downwardly and upwardly persisted at ~30 cm beneath
 249 the ice base. This abnormal layer is sometimes called a local temperature minimum (Mironov et al., 2002)
 250 or a “temperature dichotomy” (i.e., a dicothermal layer used in oceanography) (e.g., Kirillin et al., 2011,
 251 2021). Water temperature contours (not shown) revealed that both the bulk temperature and thickness of
 252 the dicothermal layer show significant diurnal cycles: its temperature and thickness take up and increase
 253 following the solar insolation cycle and decrease or even disappear during the night. The development
 254 and extension of this layer also increase the thermal gradient of the overlying interface layer.
 255 Occasional snowfall events usually led to quick bulk cooling along the entire water temperature profile
 256 due to the high reflection of new snow despite their small thickness. The sensitive response of water
 257 temperature to snow events (actually changes in penetrated radiation) implies large heat flux from water
 258 to ice and the dominance of solar radiation in this lake.



259
 260 **Figure 5. Daily profile evolution of water column during ice season of winters (a) 2016, (b) 2017,**
 261 **(c) 2018, and (d) 2019. Light blue and brown zones denote ice cover and bottom sediment,**
 262 **respectively. Asterisks (✖) denote snowfalls and snow-covered periods. Plus (+) and minus (-)**
 263 **denote the growth and melt stage of the ice cover.**

264
 265 Unconventionally, under-ice convection did not take place in all winters (only two of our four
 266 observational winters) and seems to develop just when the bulk water temperature goes up to 7°C. This
 267 temperature threshold is higher than the temperature of maximum density of freshwater (3.98°C) and
 268 saline water (<3.98°C). These annually variable convections are believed to form conditionally and lake-
 269 specifically with proper water-sediment temperature and salinity profile. When the water temperature is
 270 large enough, its density effect overcomes salinity stratification and convection is thus triggered. Taking
 271 winter of 2017 as an example, water sampling indicated that, in this very shallow lake, the salinity

272 increased and its profile structure changed simultaneously as the ice grew (Fig. 6). At the ice-on, the
 273 salinity showed a stable profile (increasing downwardly) and its impact on water density outweighed the
 274 impact of concurrent temperature gradient (i.e., on Jan 5). With the following ice growth, the bulk salinity
 275 increased but the salinity gradient decreased, and the temperature gradient decreased. Consequently, the
 276 weakened salinity gradient could persistently outweigh or offset the impact of temperature profile on
 277 water density through the growing period (before Mar 4). Otherwise, if the weakening gradient of salinity
 278 no longer offsets the temperature effect, the convective mixing takes place across the density instability
 279 layer. This is very likely why under-ice mixing occurred in the winters of 2016 and 2018. When the ice
 280 started melting, the salinity gradient turned larger due to fresh meltwater released from the top, the water
 281 column or the top layer became more stable (on Mar 11).
 282 We can conclude that how the water temperature and salinity profiles change synchronously during late
 283 freezing and initial melting determines whether the under-ice convection takes place. Especially, if the
 284 sediment temperature is high and the transmitted radiation is large during freezing, the sediment and
 285 bottom water temperature can be warm and increase rapidly, increasing the probability for full-depth
 286 convection such as in the winters of 2016 and 2018.



287
 288 **Figure 6. Observed temperature and salinity profiles and estimated water density (according to**
 289 **Leppäranta (2015)) in winter 2017.**

290

291 3.3 Heat transfer at the ice-water interface

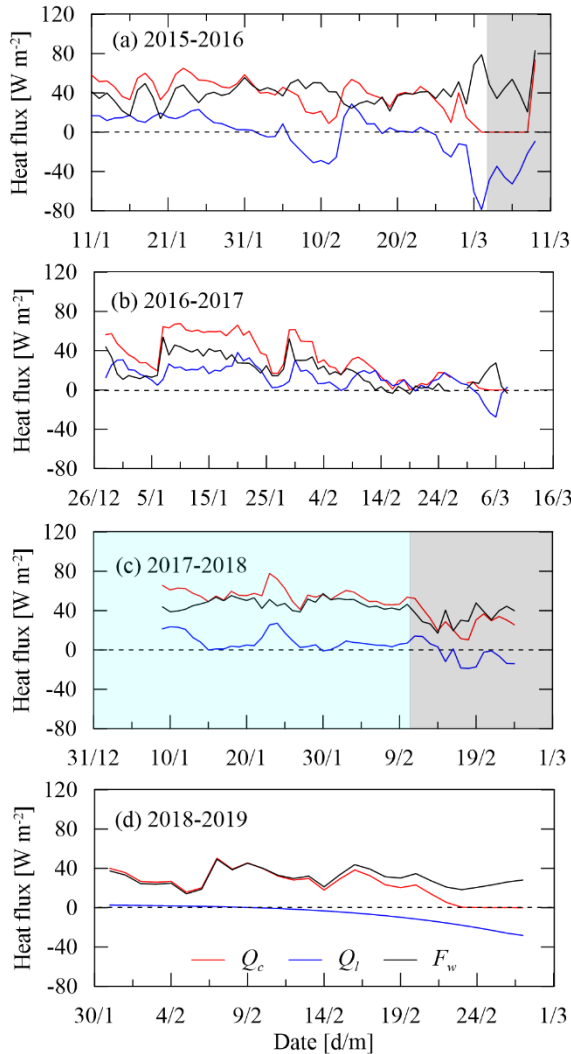
292 Heat and mass fluxes at the ice-water interface govern the basal freezing/melting rate of ice cover and
 293 the temperature of the top water layer. Our data show that in mid-winter, ice growth slowed down, and
 294 then a near-equilibrium period appeared (i.e., the thickness kept roughly constant) prior to the start of the
 295 melting period (Fig. 4). At the ice bottom, the latent heat flux Q_l kept positive during continuous ice
 296 growth and fluctuated near zero level during the near-equilibrium period. Thereafter the ice began to melt
 297 from bottom, and Q_l turned negative (Fig. 7). The conductive heat flux Q_c through the bottom ice layer
 298 kept positive, indicating upward heat transport. After the ice had started fast melting, Q_c went down to
 299 near zero with the ice cover turned into a (quasi-)isothermal state.

300 The water-to-ice heat flux F_w showed a similar variation with Q_c . Physically, F_w is crucially determined
 301 by the inverse thermal gradient of the topmost interface layer. The thinner interface layer with the higher

302 thermal gradient in winters 2016 (temporal average \pm standard deviation: $40.8 \pm 11.7 \text{ W m}^{-2}$) and 2018
 303 ($44.9 \pm 9.4 \text{ W m}^{-2}$) created higher F_w than those in winters 2017 ($21.4 \pm 12.3 \text{ W m}^{-2}$) and 2019 ($30.2 \pm 9.0 \text{ W m}^{-2}$).
 304 Interestingly, the convective mixing process increased F_w by 33% in winter 2016 but decreased F_w
 305 by 26% in winter 2018 compared with F_w before the convection occurrence, indicating complicated
 306 effects of convection.

307 During the ice growth, both latent heat due to freezing (Q_l) and conductive heat from water to ice (F_w)
 308 need to be taken out by the ice conduction heat (Q_c) (Eq. (4)). Q_c was predominantly determined by the
 309 ice thickness and surface heat balance (Leppäranta, 2015), so a higher F_w meant lower Q_l and growth
 310 rate of ice. Specifically, F_w took up $> 65\%$ of Q_c prior to the equilibrium stage (e.g., winters of 2016 and
 311 2017) and $> 90\%$ in the equilibrium stage (e.g., winters of 2018 and 2019), the remaining of Q_c was used
 312 to take the latent heat of freezing out to the atmosphere through the ice cover, leading to continuous ice
 313 growth.

314 During initial ice melting, the heat transfer from water to ice (F_w) was largely conducted through the ice
 315 cover (Q_c) (70%–80%) and partly used to melt the basal ice (Q_l). But during the following fast melting,
 316 Q_c was negligible since the isothermal ice cover depresses or even prevented heat conduction and F_w was
 317 almost totally used for basal ice melt.



318
 319 **Figure 7. Heat fluxes at the ice-water interface (Q_c : conductive heat flux in the bottom ice; Q_l : latent**
 320 **heat flux due to basal ice freezing/melting; F_w : water-to-ice heat flux). The light gray and blue**

321 zones denote periods of convective mixing and stratification with the local “warm” layer (Fig. 5),
322 respectively.

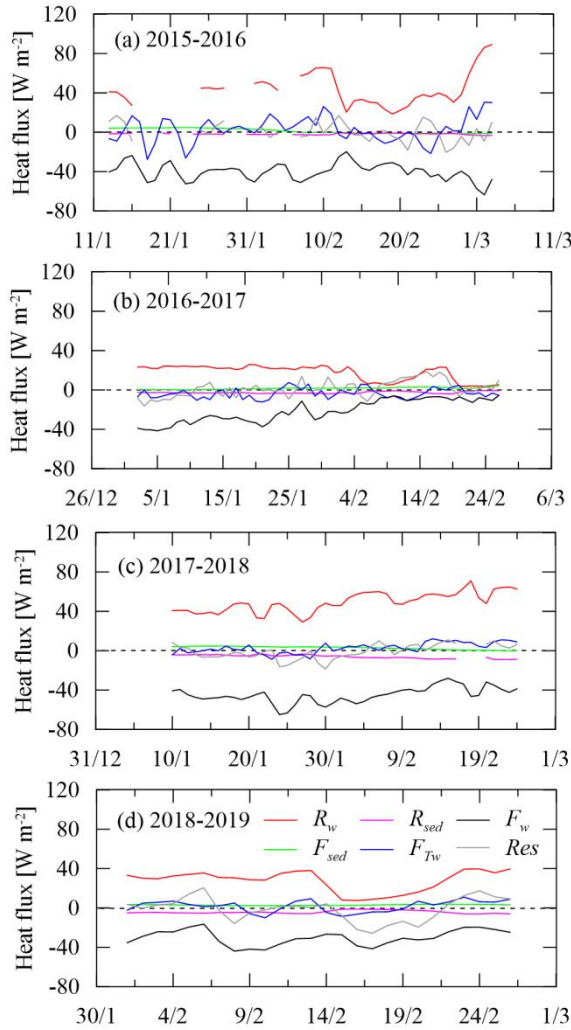
323

324 3.4 Energetics of the water column

325 The temperature regime of under-ice water is governed by the heat budget. Fig. 8 shows all the heat
326 fluxes involved and the balance residual. In mid-winter, the solar flux R_w was 25–50 W m^{-2} under bare
327 ice cover and dropped to 1.5–13 W m^{-2} under ice with a snow cover of varying thickness (1.5–8 cm) and
328 age. Only 3%–14% (1–5 W m^{-2}) of R_w (i.e., R_{sed}) reached the sediment surface (Fig. 4), which in turn
329 released heat (F_{sed}) to the overlying water in mid-winter (1–3 W m^{-2}). The heat flux from water to ice,
330 F_w , also showed interannual and seasonal variations (10–60 W m^{-2}) and was generally smaller under
331 snow-covered ice than that under bare ice, likely indicating the effect of transmitted sunlight. The heat
332 content change (F_{Tw}) of water, as a resultant heat change from heat sources and sinks, was typically small
333 ($-5 - +4 \text{ W m}^{-2}$) during freezing but grew up to 4–15 W m^{-2} during the initial melt.

334 Evidently, the transmitted solar radiation (R_w) and water-to-ice heat transfer (F_w) dominated the heat
335 balance of the under-ice water. Combining the 4-winter observations, R_w was the largest heat source
336 ($34.8 \pm 18 \text{ W m}^{-2}$) and accounted for (92±9)% of the total source ($R_w + F_{sed}$) to the under-ice water, while
337 F_w was the largest heat sink ($34.3 \pm 15 \text{ W m}^{-2}$) and accounted for (96±38)% of the total sink ($F_w + R_{sed}$).
338 The term ($F_{sed} - R_{sed}$) was only $-0.8 \pm 2.7 \text{ W m}^{-2}$ and F_{Tw} was $0.7 \pm 8.7 \text{ W m}^{-2}$, both of which can be
339 neglected compared to others. Therefore, the transmitted solar radiation was almost totally (97%)
340 returned to the ice base by means of water-to-ice heat conduction.

341 Inter-annual comparisons indicated that winter 2017 with only a prevailing inverse temperature structure
342 and a decreasing bulk temperature was different from that in other winters (Figs. 4 and 5). Heat flows
343 and budget can provide basic insight into the differences. During the freezing period of winter 2017, the
344 bulk water temperature kept decreasing because the net heat gain of water was negative (i.e. $R_w + F_{sed} -$
345 $F_w < 0$); Continuous heat loss of water to the ice bottom also created inverse thermal gradient and decrease
346 in water temperature prevented the occurrence of mixing. However, in other winters (especially 2016
347 and 2018), the net heat gain of water was positive, so the water temperature had an increasing trend,
348 which increases the potential for mixing occurrence. Compared with other winters, snow bands and spots
349 that prevailed on top of a thicker ice cover in winter 2017 caused lower penetrated solar radiation, largely
350 contributing to the general cooling of the water column.



351

352

Figure 8. Heat budget of the under-ice water (R_w : transmitted solar radiation; R_{sed} : absorbed solar radiation by sediment; F_w : water-to-ice heat flux; F_{sed} : heat released from sediment; F_{Tw} : sensible heat caused by water heat content change; Res : residual of heat balancing, which is supposed to be zero when all heat fluxes balance ideally)

355

356

357

4 Discussion

358

4.1 Comparisons with (sub)Arctic and temperate climate lakes

359

Prior to the ice-on date, in freshwater lakes fall mixing due to thermally free convection (at 3.98°C) and continuous wind stirring against weak salinity gradients usually create large/full-depth vertical isothermal structure with temperature quite close to the freezing point (stage I in Fig. 9).

362

After the freeze-up or ice-on, the under-ice stratification evolves as a joint result of snow and ice condition, solar radiation penetration into water, heat flux from the bottom sediment, and horizontal advection and diffusion. In Arctic, boreal, and northern temperate regions, such as Fennoscandia, north America, and central Europe, winter precipitation leads to thick snow cover on lake ice, and only little sunlight can penetrate through the snow and ice cover and, hence, can be neglected in the water column.

367

The water column receives heat from the bottom sediment and releases heat to the ice cover on top. These heat fluxes are small (0–5 W m⁻²), and therefore the lake water stays close to the freezing point in the top layer and has a very weak inverse structure (curve I) through the entire growth period of 3–5 months.

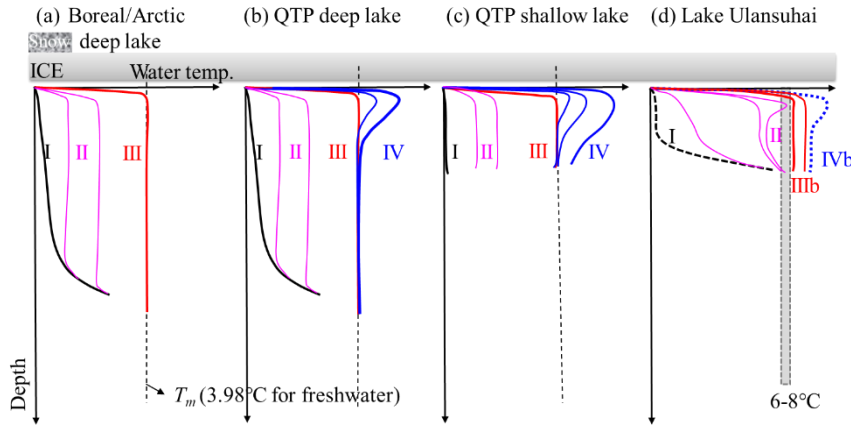
369

370 After the melting onset, warm air and strengthened solar radiation lead to snow melting, and more solar
371 radiation goes through the transparent ice and heats up the underlying water, creating a deepening
372 convective mixing (stage **II**) before reaching the temperature of maximum density (T_m) (stage **III**).
373 Usually, the ice cover breaks up before the thermal state of stage **III** forms in most deep boreal and Arctic
374 lakes (Yang et al., 2020).

375 In mid-latitude cold and arid regions, intensive solar radiation and thin snow cover allow more solar
376 energy transmittance to the water column just following the freeze-up. In the Qinghai-Tibet Plateau
377 (QTP), the water column can keep a stable state of stage **I** or start slow warming (i.e., period of stage **II**)
378 just following the freeze-up in deep lakes, and then go to stage **III**, creating mid-winter overturn (Fig.
379 9b). Afterwards, strong solar radiation due to thin ice warms continuously the top water layer (stage **IV**),
380 which exists for 4-6 weeks before breakup (Kirillin et al., 2021; Lazhu et al., 2021). However, in shallow
381 ponds, stage **II** (i.e., transition from stage **I** to **III**) is very short (one week), and the water column roughly
382 stays at stage **III** almost over the entire freezing period. The following warm layer (**IV**) can deepen to
383 near the lake bottom before ice-off (Fig. 9c) (Huang et al., 2019b).

384 Lake Ulansuhai is very shallow and weakly saline, and although the solar radiation is strong, thermal
385 stratification dynamics is determined by the synchronous profile evolution of temperature and salinity.
386 Although our observations covered only the mid-winter, the thermal profile of type **I** is expected at the
387 pre-winter and ice-on due to joint effects of wind-stirring and salinity gradient. But stage **I** should be
388 very short, and the bulk temperature increases rapidly and transition to stage **II** takes place due to the
389 solar radiation transmittance and shallow lake depth. However, the occurrence of convective mixing (we
390 used stage **IIIb** here for brackish water) is conditional and mainly dependent upon the salinity evolution
391 due to the freezing-exclusion effect. Stage **IV** is also expected since meltwater dilution in the top layer
392 can suppress the convection. Note that, the forming regime of stage **IIIb** is different in this brackish lake
393 compared with stage **III** in freshwater lakes, which are predominantly driven by temperature approaching
394 T_m with solar heating. In brackish lakes, convective mixing may be stopped by a dicothermal layer in
395 the middle (Fig. 5c) and full convection is possible only when the bottom water is warm enough to
396 conquer the salt stratification.

397 Salinity structure plays a more important role in lake stratification and convective mixing than the
398 temperature in brackish/saline and even freshwater lakes with salinity below 0.5 ppt (Kirillin and
399 Terzhevik, 2011). The present results indicated that the salt exclusion during freezing changes both the
400 total salt content and salinity structure. For instance, for a lake with a mean depth of 1.0 m, if the salinity
401 segregation coefficient is assumed 0.15 (Pieters and Lawrence, 2009; Bluteau et al, 2017), formation of
402 0.5 m ice cover can cause an increment of 70% to the water salinity. In Lake Ulansuhai, the salinity
403 increases downward at the ice-on with a large salinity gradient. Afterwards, as the ice grows, salt
404 exclusion gradually decreases the salinity gradient, making the water more prone to mix convectively.



405

406 **Figure 9. Typical thermal stratification types in ice-covered lakes: (a) deep lakes in Arctic (Jakkila**
 407 **et al., 2009), (b) deep lakes in QTP (Kirillin et al., 2021; Lazhu et al., 2021), (c) a shallow pond in**
 408 **QTP (Huang et al., 2019b), and (d) Lake Ulansuhai. The definitions of Roman numbers are**
 409 **presented in the text.**

410 4.2 What leads to high water-to-ice heat flux?

411 The water-to-ice heat flux F_w plays a predominant role in the basal growth and melting of lake ice cover
 412 but is quite challenging to observe instrumentally. Eqs. (1) and (4) provide two ways to estimate F_w
 413 indirectly if the ice thickness, temperature profile of the ice-water-sediment column, and solar irradiance
 414 are observed (actually these variables were often observed in lake thermal regime and ice programs).

415 By definition, F_w is the conductive heat flux across the very thin diffusive water layer just beneath the
 416 ice. The temperature gradient and thickness of this thin layer are influenced to a varied extent by thermal
 417 stratification, convective mixing (Figs. 5 and 6), advection (Rizk et al., 2014; Kirillin et al., 2015), and
 418 seiche oscillation (Kirillin et al., 2018). All these thermal and hydraulic processes lead to non-stationary
 419 and spatiotemporally varying F_w (Winters et al., 2019).

420 In freshwater lakes, under-ice convective mixing is observed to increase heat transport to the ice bottom
 421 by increasing the thermal gradient of the interfacial layer above the convective layer (Mironov et al.,
 422 2002; Kirillin et al., 2018). However, in weakly saline Lake Ulansuhai, under-ice convective mixing does
 423 not necessarily take place every winter and its impact on heat transport to the ice bottom differs annually.
 424 In the winter of 2016, the convective mixing developed even across the entire water column, and then
 425 encroached the overlying interfacial diffusive layer and increased the bottom temperature of this layer
 426 (Fig 5a), resulting in an increase in the thermal gradient of this layer and thus enhancing the heat diffusion
 427 (i.e., increasing F_w). However, in the winter of 2018, the convection took place only in the lower half
 428 of the water column, slightly decreased the thermal gradient of the overlying diffusive layer, and
 429 eliminated the dicothermal layer that maintained relatively high F_w prior to the convection onset
 430 (Fig 5c), leading to a decrease in F_w . In the future, detailed synchronous datasets on synchronous
 431 temperature and salinity profiles are needed to understand the accurate regime of convection in this
 432 type of lakes.

433 Although we did not acquire concurrent salinity profiles to the water temperature, sampling results in the
 434 winter of 2017 inevitably indicate the development of double diffusion as the temperature destabilizes
 435 while the salinity stabilizes the stratification (Schmitt, 1994; Schmid et al., 2010). The effective heat
 436 diffusivity of the bulk water column estimated from F_w derived by Eq. (4) was 5–16 (mean of
 437 approximately 10) times larger than the molecular diffusivity, indicating the significantly enhanced

438 diffusivity of heat due to the double diffusion.

439 In boreal and Arctic lakes, weak solar radiation, short insolation duration, and most importantly thick
440 snow cover limit solar heat input to the under-ice water column, just water and sediment heat release
441 (both very small) can cause only low seasonal values, $F_w < 15 \text{ W m}^{-2}$ (Malm et al., 1997; Jakkila et al.,
442 2009). However, in arid or mid-latitude lakes with thin snow and/or more intensive solar insolation, F_w
443 can be high, 10–50 W m^{-2} in Lake Baikal (Aslamov et al., 2017) and 20–100 W m^{-2} in QTP lakes with
444 distinct seasonal variation (Huang et al., 2019a,b; Kirillin et al., 2021). The estimated F_w in Lake
445 Ulansuhai is comparable to Lake Baikal and QTP lakes, indicative of the vital contribution of solar
446 radiation and the absence of snow cover.

447 Higher F_w does not necessarily mean growth suspend, shorter freezing duration, or thinner lake ice cover.
448 In Lake Ulansuhai, in ice growth, the conductive heat in the ice cover (Q_c) is much higher, which means
449 that the F_w can be totally released through the ice cover and the freezing latent heat (Q_l) can also be taken
450 out since $F_w + Q_l = Q_c$. This ensures the continuous growth of ice. In ice melting, the Q_c is usually
451 ignorable, the under-ice water supplies heat (F_w) to maintain basal ice melting (Q_l). Higher F_w means a
452 greater melting rate.

453 From a perspective of heat balance in water (Eq. 1),

454
$$F_w = R_w - R_{sed} + F_{sed} + F_h - \rho_w c_w h_w \frac{dT_w}{dt} - \rho_w c_w T_w \frac{dh_w}{dt}, \quad (5)$$

455 If we define $Q_{rad} = R_w - R_{sed}$ (i.e., solar absorption by the water column), and the heat content change
456 due to subsurface water seepage is negligible, Eq. (5) is transformed to

457
$$F_w = Q_{rad} + F_{sed} + F_h - F_{T_w}, \quad (6)$$

458 which means the solar energy (Q_{rad}) and sediment heat (F_{sed}) are used to change the bulk water
459 temperature (F_{T_w}) and its structure. In turn, the water body loses heat to the ice by adjusting its bulk
460 temperature and structure. R_{sed} is usually very small, so,

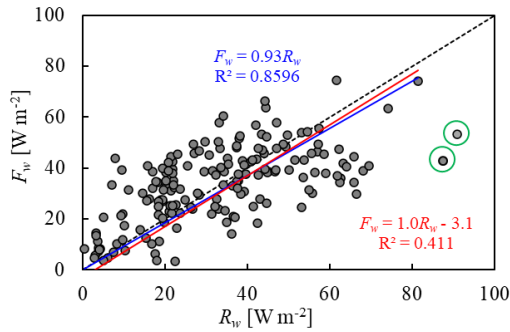
461
$$Q_{rad} \approx R_w. \quad (7)$$

462 And Eq. (6) can be transformed to a simple linear formula to present the contribution of R_w ,

463
$$F_w = aR_w + b, \quad (8)$$

464 where slope a reflects the contribution of the penetrated solar radiation while intercept b reflects the
465 integrated contributions of other heats. Fig. 8 argued that both F_{sed} and F_{T_w} are very small and roughly
466 constant and R_w and F_w are the overwhelming dominant heat source and sink, respectively. In
467 consequence, if we fit the $F_w \sim R_w$ data using $a=1$, the regressed mean contribution of heat fluxes except
468 is -3.1 W m^{-2} (red line in Fig. 10), very close to the estimate of -1.5 W m^{-2} in Section 3.4. If we ignore
469 the minor intercept, the line with $a=0.93$ explains approximately the same amount of variance in the
470 observations (blue line in Fig. 10), consistent with the observed ratio of F_w to R_w (0.97).

471 But we have to note that values of both coefficients should be lake specific. Lake depth and salinity
472 modify the changes in convective mixing depth, bulk water temperature, and temperature structure
473 caused by solar irradiance (Lazhu et al., 2021), and thus alter the relative contributions of solar radiation
474 to water heat content and to heat transfer from water to ice. For instance, in a deep lake with a mean
475 depth of 20 m in Finland, 1/3 of the transmitted solar radiation returned to ice (Leppäranta et al., 2019).



476

477

Figure 10. Linear fitting of daily water-to-ice heat flux F_w as a function of penetrated solar radiation R_w . The black dashed line denotes $F_w = R_w$. Two models were used to fit the data with two dots in green circles being removed.

479

480

5 Conclusions

481

We present the ice-covered lake thermodynamics in a mid-latitude, cold and dry region, where the climatic and hydrological environment is in distinct contrast to the Arctic, boreal, and other northern temperate regions. The ice cover is always bare or covered by only occasional thin snow patches lasting for 1–2 weeks due to the arid climate and wind blowing. The clear congelation ice cover allows 1/5–1/3 of incident solar radiation to penetrate into the water column in mid-winter, providing a background for the energetics of under-ice water. The transmitted radiation and heat transfer across the ice-water interface dominate the heat budget of the water column and are highly correlated. High water-to-ice heat flux F_w (daily averages of 20–45 W m^{-2}) was observed compared to that in (sub)Arctic and boreal lakes and takes up >90% of the solar radiation input to the under-ice water (20–50 W m^{-2}). Snow accumulations can decrease F_w due to its large albedo and light attenuation. Despite of high F_w , higher heat conduction within the ice cover (30–55 W m^{-2}) existed during the freezing period because of the persistent snow-free ice surface and created continuous basal growth of ice. In particular, the high correlation between F_w and penetrating solar radiation indicates the temporal variation of F_w , which is important for updating F_w parameterization in lake ice modelling.

495

Both bulk water temperature and its structure show diurnal, synoptical, and seasonal variations due to their quick responses to transmitted radiation and snow events because of the small lake depth. Double diffusion should surely prevail in wintertime in this shallow saline lake and strengthens the heat transport to the ice bottom because there is always cooler and fresher water overlying warmer and saltier water. Under-ice convective mixing and/or dicothormal water layer take place in some winters depending on the dynamic interaction between radiation (temperature) and salinity stratifications, which is mediated by the salt exclusion during freezing. However, details in double diffusion, convective mixing, and the effect of salt exclusion (or cryoconcentration) on water stratification in shallow ice-covered saline lakes need to be investigated in the future using high-frequency and high-resolution measurements.

504

505

Data availability. The main datasets on lake ice/snow thickness, temperatures, and transmitted solar radiation used in this paper are available at <https://zenodo.org/record/4291840> (doi: 10.5281/zenodo.4291840).

507

508

509

Author contributions. WH, ML, and ZLi conceived the study. WZ, HY, and ZLin conducted the field observations. WZ, CZ, RL, and ZLi analysed data on meteorology and ice/snow conditions. WH and ML developed and ran the model. WZ, RL, and WH calculated the heat budgets for the water column. WH

511

512 and WZ wrote the paper with contributions from all the co-authors.

513

514 *Competing interests.* The authors declare no competing interests.

515

516 *Acknowledgements.* This study was funded by the National Key Research and Development Program of
517 China (2019YFE0197600), National Natural Science Foundation of China (51979024), the Open Fund
518 of State Key Laboratory of Frozen Soil Engineering (SKLFSE201813), the Program of Introducing
519 Talents of Discipline to Universities (B08039), the Fundamental Research Funds for the Central
520 Universities (CHD) (300102291507), and Academy of Finland (333889). We are grateful to the
521 technicians of the National Ecologic Station in Lake Ulansuhai and the rest of our field team for their
522 invaluable help in field campaigns.

523

524 **References**

525 Aslamov, I.A., Kozlov, V.V., Kirillin, G.B., Mizandrontsev, I.B., Kucher, K.M., Makarov, M.M., and Granin, N.G.:

526 A study of heat transport at the ice base and structure of the under-ice water layer in southern Baikal, *Water*
527 *Resour.* 44(3), 428–441, 2017.

528 Bernhardt, J., Engelhardt, C., Kirillin, G., and Matschullat, J.: Lake ice phenology in Berlin-Brandenburg from
529 1947–2007: observations and model hindcasts, *Climatic Change*, 112, 791–817, 2012.

530 Bluteau, C. E., Pieters, R., Lawrence, G. A., The effects of salt exclusion during ice formation on circulation in
531 lakes, *Environ. Fluid Mech.*, 17, 579-590, 2017.

532 Bouffard, D., Zdorovenova, G., Bogdanov, S., Efremova, T., Lavanchy, L., Palshin, N., Terzhevik, A., Vinnå, L.,
533 R., Volkov, S., Wüest, A., Zdorovenov, R., and Ulloa, H. N.: Under-ice convection dynamics in a boreal lake,
534 *Inland Waters*, doi: 10.1080/20442041.2018.1533356, 2019.

535 Cavaliere E., and Baulch, H. M.: Denitrification under lake ice. *Biogeochemistry*, 137(3), 285-295, 2018.

536 Franz, D., Mammarella, I., Boike, J., Kirillin, G., Vesala, T., Bornemann, N., Larmanou, E., Lang, M., and Sachs,
537 T.: Lake-atmosphere heat flux dynamics of a thermokarst lake in arctic Siberia, *J. Geophys. Res.: Atmos.*, 123,
538 5222–5239. <https://doi.org/10.1029/2017JD027751>, 2018.

539 Griffiths, K., Michelutti, N., Sugar, M., Douglas, M. S. V., and Smol, J. P.: Ice-cover is the principal driver of
540 ecological change in High Arctic lakes and ponds, *PLoS ONE*, 12(3), e0172989.
541 doi:10.1371/journal.pone.0172989, 2017.

542 Huang, W., Cheng, B., Zhang, J., Zhang, Z., Vihma, T., Li, Z., and Niu, F.: Modeling experiments on seasonal
543 lake ice mass and energy balance in the Qinghai-Tibet Plateau: a case study, *Hydrol. Earth Syst. Sci.* 23, 2173-
544 3186, 2019a.

545 Huang, W., Zhang, J., Leppäranta, M., Li, Z., Cheng, B., and Lin, Z.: Thermal structure and water-ice heat transfer
546 in a shallow ice-covered thermokarst lake in central Qinghai-Tibet Plateau, *J. Hydrol.*, 578, 124122, doi:
547 10.1019/j.jhydrol.2019.124122, 2019b.

548 Huang, W., Zhang, Z., Li, Z., Leppäranta, M., Arvola, A., Song, S., Huotari, J., and Lin, Z.: Under-ice dissolved
549 oxygen and metabolism dynamics in a shallow lake: The critical role of ice and snow, *Water Resour. Res.*, 57,
550 e2020WR027990, doi: 10.1029/2020WR027990, 2021.

551 Jakkila, J., Leppäranta, M., Kawamura, T., Shirasawa, K., Salonen, K.: Radiation transfer and heat budget during
552 the ice season in Lake Pääjärvi, Finland, *Aquat. Ecol.*, 43, 681–692, 2009.

553 Karetnikov, S., Leppäranta, M., and Montonen, A.: A time series of over 100 years of ice seasons on Lake Ladoga,
554 *J. Great Lakes Res.*, 43, 979–988, 2017.

555 Kirillin, G., Aslamov, I., Leppäranta, M., Lindgren, E.: Turbulent mixing and heat fluxes under lake ice: the role of

556 seiche oscillations, *Hydrol. Earth Syst. Sci.*, 22, 6493–6504, doi:10.5194/hess-22-6493-2018, 2018..

557 Kirillin, G.B., Forrest, A.L. Graves, K.E., Fischer, A., Engelhardt, C., and Laval, B.E.: Axisymmetric circulation
558 driven by marginal heating in ice-covered lakes, *Geophys. Res. Lett.*, 42, 2893–2900, 2015.

559 Kirillin, G., Leppäranta, M., Terzhevik, A., Granin, N., Bernhardt, J., Engelhardt, C., Efremova, T., Golosov, S.,
560 Palshin, N., Sherstyankin, P., Zdorovenнова, G., and Zdorovennov, R.: Physics of seasonally ice-covered lakes:
561 a review, *Aquat. Sci.*, 74, 659–682, 2012.

562 Kirillin, G., Shatwell, T., and Wen, L.: Ice-covered lakes of Tibetan plateau as solar heat collectors, *Geophys. Res.*
563 *Lett.*, 48, e2021GL093429, 2021.

564 Kirillin, G., Terzhevik, A.: Thermal instability in freshwater lakes under ice: Effect of salt gradients or solar
565 radiation?, *Cold Reg. Sci. Technol.* 65(2), 184-190, 2011.

566 Lazhu, Yang, K., Hou, J., Wang, J., Lei, Y., Zhu, L., Chen, Y., Wang, M., and He, X.: A new finding on the
567 prevalence of rapid water warming during lake ice melting on the Tibetan Plateau, *Science Bulletin*,
568 <https://doi.org/10.1016/j.scib.2021.07.022>, 2021.

569 Leppäranta, M.: Freezing of lakes and the evolution of their ice cover, Springer, Berlin, Heidelberg, 2015.

570 Leppäranta, M., Lindgren, E., Wen, L., and Kirillin, G.: Ice cover decay and heat balance in Lake Kilpisjärvi in
571 Arctic tundra, *J. Limnol.*, 78, doi:10.4081/jlimnol.2019.1879, 2019.

572 Lei, R., Leppäranta, M., Cheng, B., Heil, P., and Li, Z.: Changes in ice-season characteristics of a European Arctic
573 lake from 1964 to 2008, *Climatic Change*, 115(3-4), 725-739, 2012.

574 Lu, P., Cao, X., Li, G., Huang, W., Leppäranta, M., Arvola, L., Huotari, J., and Li, Z.: Mass and heat balance of a
575 lake ice cover in the central Asian arid climate zone, *Water*, 12, 2888, doi:10.3390/w12102888, 2020.

576 Malm, J., Terzhevik, A., Bengtsson, L., Boverinov, P., Glinsky, A., Palshin, N., and Petrov, M.: Temperature and salt
577 content regimes in three shallow ice-covered lakes 2. Heat and mass fluxes, *Hydrol. Res.*, 28, 129–152, 1997.

578 Mironov, D., Terzhevik, A., Kirillin, G., Jonas, T., Malm, J., Farmer, D.: Radiatively-driven convection in ice-
579 covered lakes: Observations, scaling and mixed-layer model, *J. Geophys. Res.*, 107(C4), 3032, doi:
580 10.1029/2001JC000892, 2002.

581 Pieters, R., Lawrence, G. A.: Effect of salt exclusion from lake ice on seasonal circulation, *Limnol. Oceanogr.*, 54(2),
582 401-412, 2009.

583 Ptak, M., Sojka, M., and Nowak, B.: Effect of climate warming on a change in the thermal and ice conditions in the
584 largest lake in Poland-Lake Śniardwy, *J. Hydrol. Hydromech.*, 68(3), 260-270, 2020.

585 Rizk, W., Kirillin, G., and Leppäranta, M.: Basin-scale circulation and heat fluxes in ice-covered lakes, *Limnol.*
586 *Oceanol.*, 59(2), 445–464, 2014.

587 Shi, L., Li, Z., Niu, F., Huang, W., Lu, P., Feng, E., Han, H.: Thermal diffusivity of thermokarst lake ice in Beiluhe
588 basin of the Qinghai-Tibet Plateau, *Ann. Glaciol.*, 55(66), 153-158, 2014.

589 Schmid, M., Busbridge, M., Wüest, A.: Double-diffusive convection in Lake Kivu, *Limnol. Oceanogr.*, 55(1), 225-
590 238, 2010.

591 Schmitt, R. W.: Double diffusion in oceanography, *Ann. Rev. Fluid Mech.*, 26(1), 255–285, 1994.

592 Song, S., Li, C., Shi, X., Zhao, S., Tian, W., Li, Z., Bai, Y., Cao, X., Wang, Q., Huotari, J., Tulonen, T., Uusheimo,
593 S., Leppäranta, M., Loehr, J., and Arvola, L.: Under-ice metabolism in a shallow lake in a cold and arid climate,
594 *Freshwater Biol.*, <http://doi.org/10.1111/fwb.13363>, 2019.

595 Sun, B., Li, C. Y., Cordovil, C. M. D. S., Jia, K. L., Zhang, S., de Varennes, A., and Pereira, L. S.: Variability of
596 water quality in Ulansuhai Lake receiving drainage water from Hetao Irrigation system in Yellow River Basin,
597 China, *Fresen. Environ. Bull.*, 22(6), 1666-1676, 2013.

598 Sun, B., Li, C. Y., and Zhu, D. N.: Changes of Ulansuhai Lake in past 150 years based on 3S technology,
599 *International Conference on Remote Sensing IEEE*, doi:10.1109/rsete.2011.5964944, 2011.

600 Verpoorter, C., Kutser, T., Seekell, D. A., and Tranvik, L. J.: A global inventory of lakes based on high-resolution
601 satellite imagery, *Geophys. Res. Lett.*, 41(18), 6396-6402, 2014.

602 Volkov, S., Bogdanov, S., Zdorovenov, R., Zdorovenova, G., Terzhevik, A., Palshin, N., Bouffard, D., and
603 Kirillin, G.: *Environ. Fluid Mech.*, 19, 751-764, 2019.

604 Wang, B., Ma, Y., Chen, X., Ma, W., Su, Z., and Menenti, M.: Observation and simulation of lake-air heat and
605 water transfer processes in a high-altitude shallow lake on the Tibetan Plateau, *J. Geophys. Res. Atmos.*, 120, 12
606 327–12 344, 2015.

607 Winters, K. B., Ulloa, H. N., Wüest, A., and Bouffard, D.: Energetics of radiatively heated ice-covered lakes,
608 *Geophys. Res. Lett.*, 45, 8913-8925, 2019.

609 Yang, B., Wells, M. G., McMeans, B. Dugan, H. A., Rusak, J. A., Weyhenmeyer, G. A., Brentrup, J. A., Hryciak, A.
610 R., Laas, A., Pilla, R. M., Austin, J. A., Blanchfield, P. J., Carey, C. C., Guzzo, M. M., Lottig, N. R., Mackay,
611 M. D., Middel, T. A., Pierson, D. C., Wang, J., and Young, J. D.: A new thermal categorization of ice-covered
612 lakes, *Geophysical Research Letters*, doi: 10.1029/2020GL091374, 2020.

613 Yang, F., Cen, R., Feng, W., Zhu, Q., Leppäranta, M., Yang, Y., Wang, X., Liao, H.: Dynamic simulation of nutrient
614 distribution in lakes during ice cover growth and ablation, *Chemosphere*, 281, 130781,
615 <https://doi.org/10.1016/j.chemosphere.2021.130781>, 2021.

616 Yang, F., Li, C., Leppäranta, M., Shi, X., Zhao, S., and Zhang, C.: Notable increases in nutrient concentrations in a
617 shallow lake during seasonal ice growth, *Water Sci. Technol.*, 74(12), 2773-2883, 2016.

618 Zhu, D. N., Cathryn, R. M., Sun, B., and Li, C. Y.: The influence of irrigation and Ulansuhai Lake on groundwater
619 quality in eastern Hetao Basin, Inner Mongolia, China, *Hydrogeol. J.*, 22 (5), 1101-1114, 2014.